Catalysis
Science &
Technology

Methanation of CO2 and reverse water gas shift reactions on Ni/SiO2 catalysts: The influence of particle size on selectivity and reaction pathway

Complete List of Authors:	Chen, Ching-Shiun; Chang Gung University, Center for General Education Wu, Hung-Chi; National Tsing Hua University, Materials Science and Engineering Chang, Yu-Ching; Taiwan Power Research Institute, Wu, Jia; Chang Gung University, Center for General Education Lin, Jarrn-Horng; National University of Tainan, Department of Materials Science Lin, I-Kuan; National University of Tainan, Department of Materials Science

SCHOLARONE™
Manuscripts

Catalysis Science & Technology

ARTICLE

Methanation of CO_2 and reverse water gas shift reactions on Ni/SiO$_2$ catalysts: The influence of particle size on selectivity and reaction pathway

H.C. Wu [a], Y.C. Chang [b], J.H. Wu [a], J.H. Lin [c], I.K. Lin [c], C.S. Chen [a,*]

Catalytic CO_2 hydrogenation has been studied on both 0.5 wt% and 10 wt% Ni/SiO$_2$ catalysts with particular focus on the production of CO and CH_4. The large difference in Ni particle size between the 0.5 wt% and 10 wt% Ni loadings strongly affects the kinetic parameters of CO_2 hydrogenation, the formation pathways of CO and CH_4, and the reaction selectivity. The consecutive and parallel reaction pathways show preferences for small Ni clusters and large Ni particles, respectively. At low Ni loading (0.5 wt%), the catalyst shows a comparatively higher catalytic activity for CO_2 hydrogenation with high CO selectivity. With Ni loading increased to 10 wt% (ca. 9-nm particles), the selectivity is switched to favor CH_4 formation. A formate species in a monodentate configuration is intricately involved in CO_2 hydrogenation on both Ni/SiO$_2$ catalysts, regardless of the Ni loading and particle size. The consecutive pathway, which is favored on small Ni particles, is attributed to low H_2 coverage on the Ni surface, leading to dissociation of formate intermediates resulting in CO formation and high CO selectivity. The reaction of CO_2 hydrogenation on large Ni particles may be controlled by mixed consecutive and parallel pathways, providing the likelihood that the formate intermediate is competitively hydrogenated to CO or CH_4 as part of a parallel reaction pathway. The sites corresponding to kink, corner or step positions on the Ni/SiO$_2$ surface are proposed as the primary active sites for CO_2 hydrogenation.

1.Introduction

Carbon dioxide, which is primarily generated from combustion, is the most important and abundant greenhouse gas and is the main contributor to the greenhouse effect. The recycling of CO_2 as a carbon source for catalytic chemical synthesis is one of the most promising opportunities for CO_2 utilization.[1] Currently, hydrogenation of CO_2 is widely used in the production of organic compounds, such as formic acid, methanol, carbon monoxide, methane, and hydrocarbons.[2-30] However, these processes may involve the co-formation of CO and CH_4, usually attributed to the first step of CO_2 hydrogenation on solid metal catalysts.[31-37] Reports in the literature indicate that the heterogeneous hydrogenation of CO2 usually results in CO production with high efficiency via the reverse water gas shift (RWGS) reaction ($H_2+CO_2 \rightarrow CO+H_2O$). The RWGS reaction may be directly or indirectly relevant to several industrial catalytic technologies, such as methanol synthesis, methane reforming with carbon dioxide, ammonia synthesis, the Fischer-Tropsch reaction, and steam

reforming of hydrocarbons.[38-45] Alternatively, the methanation of CO_2 ($4H_2+CO_2 \rightarrow CH_4+2H_2O$), also called the Sabatier reaction, has recently attracted significant attention due to interest in the development of renewable carbon sources and sustainable processes.[22,33-36] The Sabatier reaction is thermodynamically favorable (ΔG^o=-130.8 kJ/mol), but the high kinetic barrier associated with the conversion is still problematic for industrial applications. Fundamental studies into increasing the activity and selectivity of CH_4 production have been reported in the literature. The factors studied include the role of the support and methods for kinetic control of the CO/CH_4 selectivity and the reaction mechanism.[31-35] Several transition metals, such as Ni, Ru, Rh, Pd, Pt, Cu and bimetallic alloys, have been used as active catalysts in CO_2 hydrogenation, including both RWGS and CO_2 methanation reactions.[31-36] The effects of the partial pressure of H_2 and metal particle size are frequently discussed as factors in the control of CO/CH_4 selectivity during CO_2 hydrogenation.[31-33,36] The CO/CH_4 selectivities of reactions with Ni, Ru and Pd catalysts have been shown to be sensitive to the particle size.[31,32,36] A high H_2 concentration may aid in the attainment of high CH_4 yields.[33,36] It is generally thought that small particle sizes induce a high rate of CO formation, while the selectivity for CH_4 is enhanced on large metal particles.[31,32] However, the fundamental reasons that the particle size promotes selectivity for CO or CH_4 has attracted little attention. Nickel is known to be highly active in various catalytic hydrogenation processes. Because noble metals are a scarce, expensive resource, inexpensive Ni metal is an

attractive substitute due to its low price and current widespread use. In this paper, SiO_2-supported Ni particles of different sizes were used to study CO_2 hydrogenation. This work is devoted to the study of the mechanism, reaction pathway and selectivity promoted by different Ni particle sizes. In particular, the correlation between reaction pathway and selectivity are discussed in depth.

Results

3.1 Characterization of Ni/SiO$_2$ catalysts

Figure 1 shows the XRD patterns of the 0.5 wt% and 10 wt% Ni/SiO$_2$ materials. The 10 wt% Ni/SiO$_2$ catalyst showed peaks at $2\theta=44.3°$, $51.7°$, $76.4°$, $92.8°$ and $98.4°$ corresponding to the (111), (200), (220), (311) and (222) facets, respectively. The XRD signals of 0.5 wt% Ni/SiO$_2$ were too weak to discriminate from the background. The average particle size of the reduced 10 wt% Ni/SiO$_2$ samples (~9 nm) was calculated from the Ni(111) peak according to the Scherrer equation using the full-width at half maximum (fwhm) values, as shown in Table S1. The Ni surface areas of the Ni/SiO$_2$ catalysts used in the experiments were measured via saturated CO chemisorption at room temperature, as summarized in Table S1.

(a)

(b)
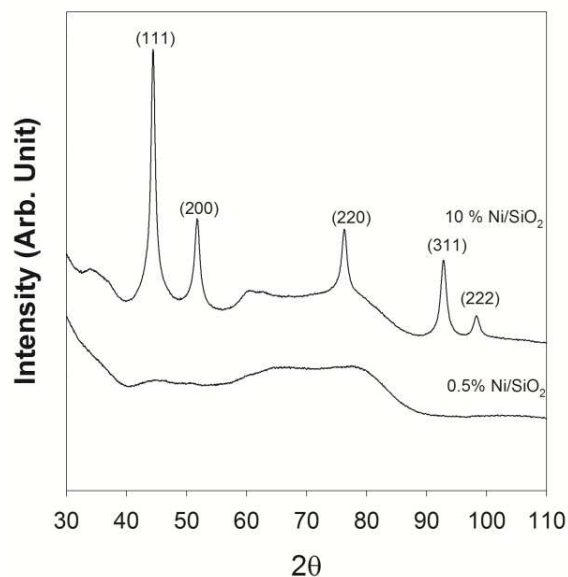
Fig.1 XRD spectra of the 0.5 wt% and 10 wt% Ni/SiO$_2$ catalysts.

HRTEM images of the Ni/SiO$_2$ catalysts are shown in Figure 2. For the 0.5 wt% Ni/SiO$_2$, tiny particles, similar to atomically dispersed Ni, were observed on the SiO$_2$. This finding provided an explanation as to why no detectable XRD patterns could be found for the 0.5 wt% Ni/SiO$_2$ material. As the Ni loading increased to 10 wt%, large, non-uniform Ni particles were observed on the SiO$_2$.
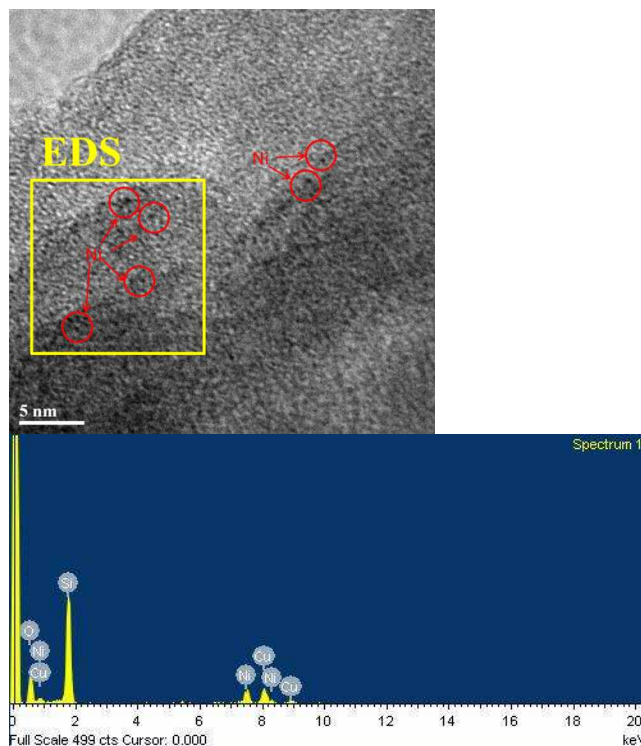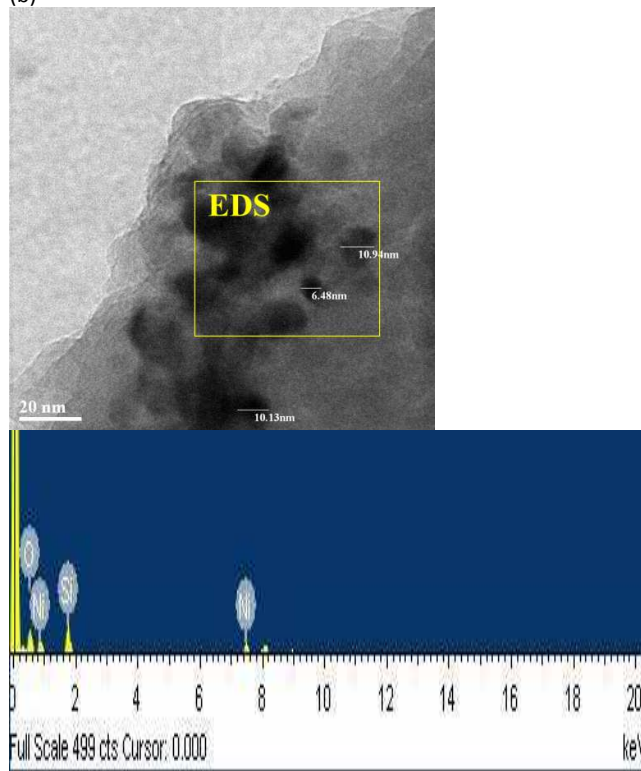
Fig. 2 HRTEM images and EDS spectra of (a) 0.5 wt% Ni/SiO$_2$ and (b) 10 wt% Ni/SiO$_2$.

The H$_2$-TPR profiles of the samples containing Ni^{2+} impregnated in SiO$_2$ and calcined at 673 K for 5 h are shown in Figure 3. The reduction of the NiO species was observed over a wide temperature range (473-813 K). Consistent with previous reports, the peak at lower temperature (<673 K) was attributed to the reduction of large NiO particles, while the peak at higher temperatures is a result of the reduction of smaller NiO particles or NiO particles with strong support interactions.[46] However, the reduction pretreatment performed at 773 K should fully reduce the Ni particles on the SiO$_2$ support.
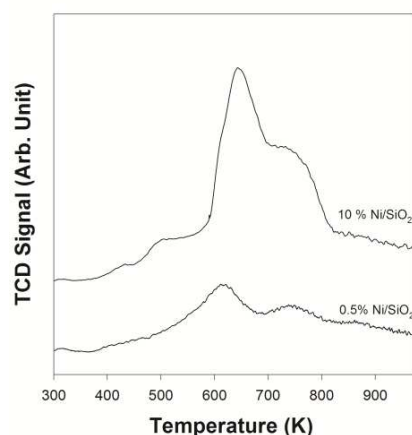
Fig. 3 H$_2$-TPR profiles of 0.5 wt and 10 wt% Ni/SiO$_2$.

3.2 Tests of catalytic CO$_2$ hydrogenation on the Ni/SiO$_2$ catalysts

The major products detected during CO$_2$ hydrogenation were CO and CH$_4$. Figure 4 compares the dependence of the specific turnover frequency (TOF) on the overall conversion of CO$_2$ hydrogenation (panel A), production of CO (panel B) and production of CH$_4$ (panel C) as a function of temperature for both Ni/SiO$_2$ catalysts. The overall activity for CO$_2$ conversion and the TOF value for CO formation on the 0.5 wt% Ni/SiO$_2$ catalyst were much higher than on the 10 wt% Ni/SiO$_2$ catalyst at all temperatures. However, the 10 wt% Ni/SiO$_2$ catalyst provided better catalytic activity in terms of CH$_4$ formation than the 0.5 wt% Ni/SiO$_2$ catalyst.
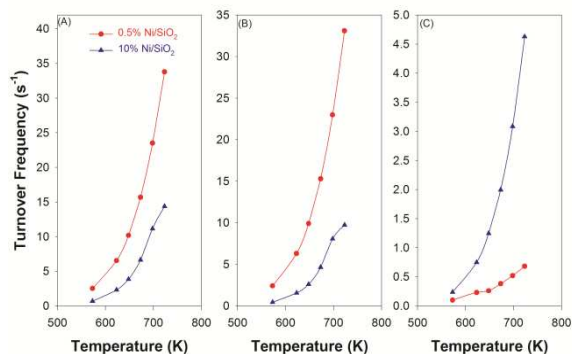
Fig. 4 Comparison between the CO$_2$ hydrogenation temperature-dependent turnover frequencies for the 0.5 wt% and 10 wt% Ni/SiO$_2$ catalysts: (A) overall CO$_2$ conversion; (B) CO formation and (C) CH$_4$ formation. The H$_2$/CO$_2$ stream with 1/1 ratio at a total flow rate of 100 ml/min passed over 50 mg of catalysts.

The relevant kinetic data for the CO$_2$ hydrogenation on the Ni/SiO$_2$ catalysts were further investigated. Arrhenius plots provide the apparent activation energies for CO$_2$ hydrogenation (Figure 5A). The apparent activation energies for the overall CO$_2$ reduction between 573 and 673 K on the Ni catalysts were estimated from the slopes, giving 57.3 kJ/mol for 0.5 wt% Ni/SiO$_2$ and 72.6 kJ/mol for 10 wt% Ni/SiO$_2$. The apparent activation energies for CO and CH$_4$ formation obtained from the Arrhenius plots in this study are compared in Figure S1. The activation energy for CO formation was ~59 kJ/mol, regardless of Ni loading. Interestingly, the E$_a$ value of CH$_4$ formation was 43.1 kJ/mol for 0.5 wt% Ni/SiO$_2$ and 69.4 kJ/mol for 10 wt% Ni/SiO$_2$. Figures 5B and 5C show the dependence of the intrinsic TOF in CO$_2$ hydrogenation versus the partial pressures of CO$_2$ and H$_2$ at 673 K on the 0.5 wt% and 10 wt% Ni/SiO$_2$ catalysts. The apparent reaction order for CO$_2$ and H$_2$ on the 0.5 wt% Ni/SiO$_2$ catalyst was determined to be ~0.5 for CO$_2$ and ~0.3 for H$_2$. This implied a possible 0.5-order dependence on both H$_2$ pressure and CO2 pressure. Interestingly, the rate law of CO$_2$ hydrogenation on the 10 wt% Ni/SiO$_2$ catalyst was determined to be $r = kP_{CO_2}^{0.06}P_{H_2}^{1.1}$, displaying a near-first-order dependence on H$_2$ pressure and a zero-order dependence on CO$_2$ pressure.
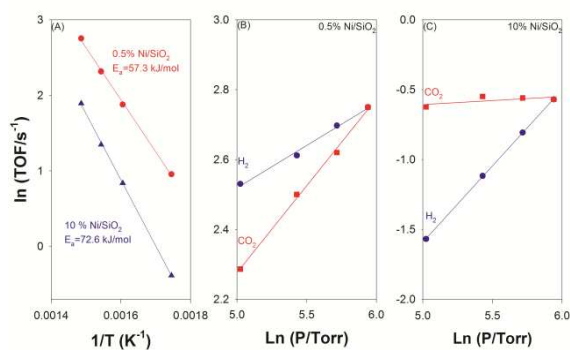
Fig. 5 (A) Arrhenius plots for the TOF of CO$_2$ hydrogenation on Ni/SiO$_2$ catalysts; (B) and (C) dependence of the ln(TOF) versus ln(P$_{H2}$) and ln(P$_{CO2}$) for the 0.5 wt% and 10 wt% Ni/SiO$_2$ catalysts.

One possible explanation for the significant differences in the reaction orders of reactants and activation energies observed with the Ni catalysts might revolve around the dramatically different Ni particle sizes resulting from the different Ni loadings. The large difference in particle size might cause fundamental changes in the selectivity and reaction pathway. Figure 6 compares the selectivity of products on both Ni/SiO$_2$ catalysts at 623 K. The total conversions in the CO$_2$ reduction reactions, for the purposes of this comparison, were controlled at ~10%. The large Ni particles present at 10 wt% loading effectively enhanced the CH$_4$ selectivity.
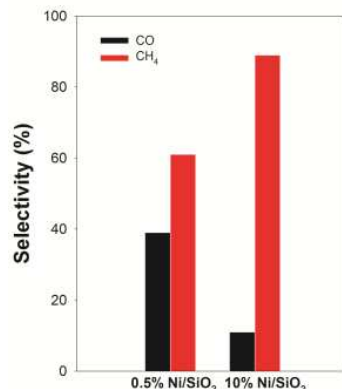
Fig. 6 Comparison of the reaction selectivity on 0.5 wt% and 10 wt% Ni/SiO_2 catalysts at 623 K. In this comparison, all CO_2 conversions were controlled at ca ~10%.

Figure 7 shows the CH_4 selectivity versus CO_2 conversion on the reduced Ni/SiO_2 catalysts. The conversion of CO_2 was controlled by varying the flow rate of the reactants (100-300 mL/min) and the amount of catalyst used in the reactions (3-20 mg). The selectivity of CH_4 decreased with decreasing conversion on the 0.5 wt% Ni/SiO_2 catalyst, with values approaching zero at zero conversion. Interestingly, the CH_4 selectivity at low conversion, when extrapolated to zero conversion, was a non-zero value at the increased 10 wt% Ni loading. For the 0.5 wt% Ni/SiO_2 catalyst, the CH_4 selectivity approached approximately zero at very low conversion, indicative of a typical stepwise reaction in which CO was an intermediate in the process of CH_4 formation.[47] In contrast, CH_4 formation on the 10 wt% Ni/SiO_2 catalyst showed 23% selectivity, even as the reaction approached zero conversion, suggesting that CO may not function as an intermediate in CH_4 production. The formation of CO and CH_4 on the 10 wt% Ni/SiO_2 catalyst might depend on a parallel reaction pathway where formation of CH_4 occurs via direct hydrogenation of CO_2.[47]
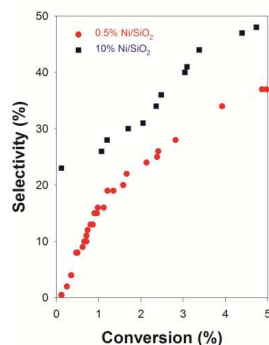
Fig. 7 Comparison of the CH_4 selectivity versus reaction conversion on the 0.5 wt% and 10 wt% Ni/SiO_2 catalysts at 623 K.

3.3 IR spectra of H_2 and CO_2 co-adsorbed on Ni/SiO_2

Figure 8 displays the IR spectra of H_2 and CO_2 co-adsorbed on the 10 wt% Ni/SiO_2 catalyst at increasing temperatures. All experiments were performed by passing a pure CO_2 stream (20

mL/min) over the catalysts for 20 min at 298 K, followed by purging with a He stream (20 mL/min). The IR spectra were recorded to monitor the adsorbed CO_2 on the Ni/SiO_2 surface under a H_2 stream at elevated temperatures. An intense IR peak at 2338 cm^{-1} was observed at 298 K. The IR band at 2338 cm^{-1}, which corresponds to adsorbed CO_2, rapidly diminished with increasing temperature. The peak at 2338 cm^{-1} was assigned to the asymmetric stretching (ν_{as}) mode of linearly adsorbed CO_2. The characteristic bands of a formate species positioned at 1297, 1625, 2850 and 2956 cm^{-1} were present at 298 K. The absorption at 1297 and 1625 cm^{-1} can be assigned to the $\nu_s(OCO)$ and $\nu_{as}(OCO)$ modes, respectively.[48-52] The peak at 2850 cm^{-1} is attributed to the $\nu(CH)$ of the formate species.[48-52] The band at 2956 cm^{-1} may be associated with a combined band representing the coupling of $\delta(CH)$ and $\nu_s(OCO)$.[52] When the temperature was elevated to 473 K, the appearance of adsorbed CO at ~2059 cm^{-1} was observed, accompanying the disappearance of the characteristic formate peaks. In general, the three possible configurations for adsorbed formate have been reported: monodentate, bidentate and bridging.[51] The frequency difference ($\Delta\nu$) between $\nu_{as}(OCO)$ and $\nu_s(OCO)$ was used to discriminate between the configurations. A monodentate configuration likely has a $\Delta\nu$ value larger than 220 cm^{-1}.[51] The configuration can be assigned as either bidentate or bridging when $\Delta\nu$ is close to, or less than, 220 cm^{-1}. This $\Delta\nu$ of 328 cm^{-1} suggested that the formate intermediate prefers the monodentate configuration. The generation of a CO stretch at ~2059 cm^{-1} may be associated with the disappearance of the monodentate formate. Similar results were observed in experiments involving the co-adsorption of H_2 and CO_2 on 0.5 wt% Ni/SiO_2 (Figure S2). The same IR experiment was also performed on pure SiO_2 (Figure S3), which could see weak CO_2 adsorption but no observable formate species was present as H_2 and CO_2 coadsobed on SiO_2.
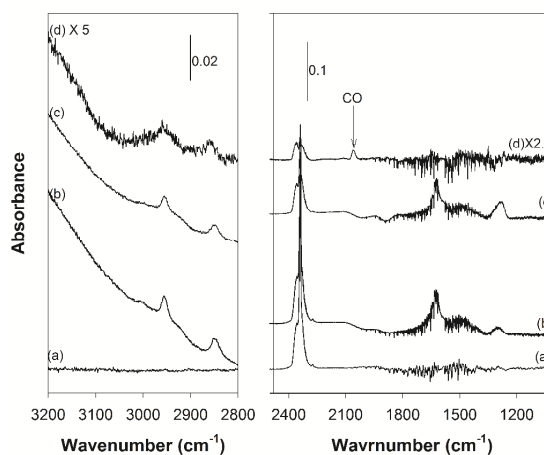
Fig. 8 IR spectra of H_2 and CO_2 co-adsorbed on the 10 wt% Ni/SiO_2 catalyst at various temperatures: (a) a pure CO_2 stream (20 mL/min) over the catalysts for 20 min at 298 K, followed by purging the CO_2 with a He stream (20 mL/min) and the adsorbed CO_2 on Ni/SiO_2 under a H_2 stream at (b) 298 K; (c) 373 K and (d) 473 K.

3.4 Measurement of temperature-programmed desorption (TPD)

Figure 9 compares the TPD profiles of CO_2 desorbed from both Ni/SiO_2 catalysts. CO_2 desorbed at ~360 and 400 K from the 0.5 wt% Ni/SiO_2 catalyst. As the Ni loading increased to 10 wt%, a new peak that is associated with CO_2 desorption appeared at 475 K, while the low temperature CO_2 desorption occurred with a similar intensity as found with the 0.5 wt% Ni/SiO_2 catalyst. The H_2-TPD results are shown in Figure 10 and reveal that H_2 desorbed from 10 wt% Ni/SiO_2 in the range of 400-540 K with a center at 445 K. However, the desorption intensity of H_2 was too weak to detect in the mass spectrometer when the same experiment was performed on the 0.5 wt% Ni/SiO_2.
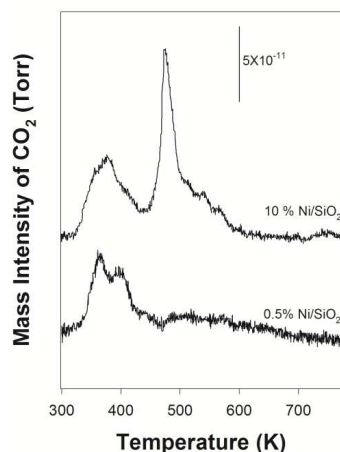
Fig. 9 TPD spectra of CO_2 desorbed from the 0.5 wt% and 10 wt% Ni/SiO_2 catalysts in a He stream at a 10 K/min heating rate. CO_2 adsorption was performed in a pure 100 mL/min CO_2 stream at atmospheric pressure and 298 K for 40 min.
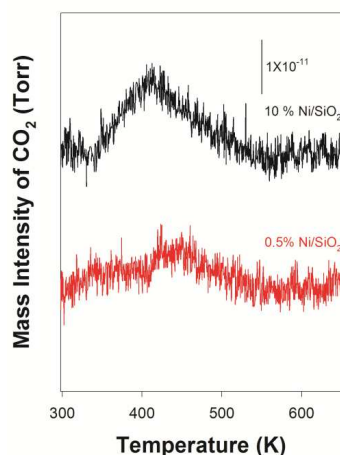
Fig. 10 TPD spectra of H_2 desorbed from the 0.5 wt% and 10 wt% Ni/SiO_2 catalysts in a He stream at a 10 K/min heating rate. The H_2 adsorption was performed in a pure 100 mL/min H_2 stream at atmospheric pressure and 298 K for 40 min.

As shown in Figure 8, the IR spectra of co-adsorbed CO_2 and H_2 on Ni/SiO_2 indicated that a formate species in the monodentate configuration might be the predominant intermediate during CO_2 hydrogenation. Thus, we used TPD to

further investigate the correlation between the formation of the products (CO and CH_4) and the formate species. The post-reaction TPD profiles of CO_2, CH_4 and CO desorbed from the 10 wt% and 0.5 wt% Ni/SiO_2 materials are shown in Figures 11A and 11B, respectively. All of the Ni catalysts were treated with a mixture of CO_2 and H_2 for 5 h at 723 K and cooled to room temperature under CO_2/H_2 stream, and then the residual gas in the system was purged with a He stream. Simultaneous desorption of CO_2, CH_4 and CO from the 10 wt% Ni/SiO_2 at ~525 K was observed. However, when the experiment was performed on the 0.5 wt% Ni/SiO_2 catalyst, the major desorbed products were CO_2 and CO. No detectable CH_4 could be observed in this course of this experiment with the 0.5 wt% Ni/SiO_2. The TPD profiles in Figure 11 may correlate to the selectivity differences between the two Ni/SiO_2 catalysts, indicating that the formation of CH_4 in CO_2 hydrogenation may be enhanced by larger Ni particles. No signal of H_2 desorbed from both Ni/SiO_2 catalysts can be observed in Figure 11.
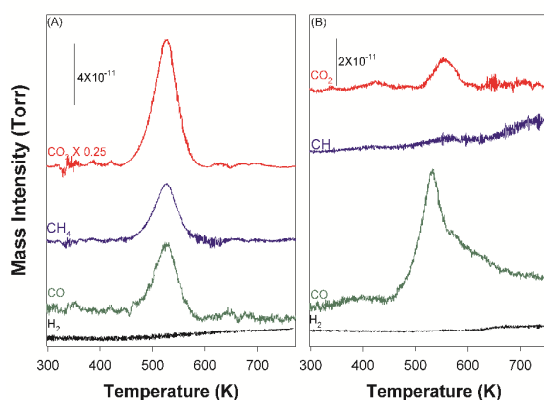
Fig. 11 TPD spectra of CO_2, CO and CH_4 in a He stream after the H_2/CO_2 (1/1) mixture was exposed to the (A) 10 wt% and (B) 0.5 wt% Ni/SiO_2 catalysts at 723 K for 5 h.

As shown in Figure 11, the temperature of CO_2 desorption was higher than that of pure CO_2 desorbed from Ni/SiO_2 (Figure 9), implying that CO_2 formation results from the dissociation of intermediates from the Ni surface. Figure S4 depicts the TPD profiles of the materials formed by formic acid (HCOOH) adsorption on 10 wt% and 0.5 wt% Ni/SiO_2. The profiles show that CO_2, CO, CH_4, H_2 and HCOOH were simultaneously desorbed at ~510 K. The formation of CO_2, CO, CH_4 and H_2 likely arise from the decomposition of a formate species present because of the adsorption of formic acid. However, the relative intensities of CH_4 and CO in both the TPD profiles showed a ratio of 0.56 for 10 wt% Ni/SiO_2 and 0.06 for 0.5 wt% Ni/SiO_2, implying that the transformation of adsorbed formic acid to CH_4 is extremely small on the small Ni particles.

3. Discussion

The TOF of CO_2 hydrogenation on the small Ni clusters on the 0.5 wt% Ni/SiO_2 was much higher than on the 10 wt% Ni/SiO_2 catalysts containing larger (9 nm) Ni particles. Recently, Pt catalysts composed of sub-nanosized particles or single atoms

showed extremely high activities for toluene oxidation, CO oxidation and PROX reactions.[53,54] The investigation of benzene steam reforming on Rh catalysts indicated that small Rh clusters caused benzene decomposition on the material surface, enhancing the catalytic reactivity.[55] In all, this literature suggests that very small and/or single-atom metal catalysts may positively enhance catalytic efficiencies. Our previous paper has reported that the sub-nanosized Pt cluster can enhance the efficiency of catalytic toluene oxidation.[56]

The dramatic change in the Ni particle size caused by the Ni concentration strongly affects the reaction selectivity of the CO_2 hydrogenation. Literature reports on the effect of the metal particle size with Ni, Ru and Pd catalysts for CO_2 hydrogenation indicate that CO formation was favored on small particles and/or single atoms and that large catalyst particles led to a significant enhancement of CH_4.[31-33] The reaction pathways for the formation of CO and CH_4 have been studied on different metal catalysts. On Ru/Al_2O_3 catalysts, the RWGS and methanation reactions were assumed to follow different routes, regardless of the Ru particle size.[31] The CO_2 hydrogenation reported on Pd- and Ni-based catalysts is proposed to follow a consecutive pathway, where CO is the key intermediate in CO_2 methanation.[32,33] The intermediate associated with CH_4 formation on Pd and Ni is still a subject of speculation. One possible suggestion is that the formation of CH_4 may strongly depend on C-O bond breaking.[57] The active carbon species generated by dissociation of CO were hydrogenated stepwise to generate CH_4, implicating a CH_x species as the reaction intermediate.[33] An alternative suggestion postulates that a formyl (HCO) species derived from the association of hydrogen and CO is the intermediate in CO methanation.

In this study, the product selectivity was found to be strongly dependent upon the size of the Ni particles. The dependence of the product selectivity versus reaction conversion (Figure 7) clearly shows that the consecutive and parallel reaction pathways may occur on small Ni clusters and large Ni particles, respectively. This suggests that different reaction pathways may result in selectivity differences and in different kinetic parameters for CO_2 hydrogenation. The possible reaction network of CO_2 hydrogenation can be described:

(1) $H_2+CO_2 \rightarrow CO+H_2O$
(2) $3H_2+CO \rightarrow CH_4+H_2O$
(3) $4H_2+CO_2 \rightarrow CH_4+2H_2O$
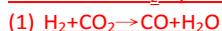
The dependences of CH_4 selectivity and conversion (Figure 7) under a kinetic regime were processed to obtain simplified equations of the consecutive and parallel reaction pathways (Appendix in ESI) that obtained $S_{CH4}=k_3/(k_1+k_3)$ for a parallel pathway and $S_{CH4}=(k_2/k_1)X_{CO2}$ for a consecutive pathway. The X_{CO2} implies CO_2 conversion. According to the equation, $S_{CH4}=(k_2/K_1)X_{CO2}$, the selectivity of CH_4 for $X_{CO2} \rightarrow 0$ should approach zero value, when the reaction follows a consecutive pathway. On the other hand, we can obtain the dependence between rate constant and both activation energies with

$$\frac{k_2}{k_1} \propto \exp(E_1-E_2)/RT$$ in the reaction in consecutive pathway

($A \xrightarrow{k_1} B \xrightarrow{k_2} C$).[58] The production of C, the final product, would increase with increasing reaction temperature if $E_1 > E_2$. The rate of CH_4 formation on 0.5 wt% Ni/SiO_2 catalyst increased with temperature (Figure 4), and the activity energies were obtained to have 58.5 kJ/mol for CO formation and 43.1 kJ/mol for CH_4 formation (Figure S1). The reaction occurred on the 0.5 wt% Ni/SiO_2 catalyst can explain satisfactorily following the consecutive mechanism. The reactions on small Ni clusters may tend to follow the consecutive pathway where CH_4 formation is mainly derived from CO hydrogenation and dependent on H_2 and CO_2 concentration to the one-half power.

On the 10 wt% Ni/SiO_2 catalyst, activation energies of CO formation was less than that of CH_4 formation, suggesting that CO_2 hydrogenation may be not completely controlled by the consecutive pathway. In Figure 7, the selectivity of CH_4 decreased with conversion decreased, but it extrapolated to make non-zero selectivity at zero conversion. However, $S_{CH4}=k_3/(k_1+k_3)$ has been given for a parallel reaction, implying that the selectivity of CH_4 should be remain constant, regardless of conversion. Therefore, it was suggested that the reaction of CO_2 hydrogenation on 10 wt% Ni/SiO_2 catalyst may be dominated by mixed consecutive and parallel pathways. The mixed consecutive and parallel pathways on large Ni particles led to a reaction rate insensitive to CO_2 concentration, with a near first-order dependence on H_2 pressure. The reaction pathways of CO_2 hydrogenation on both Ni/SiO_2 were developed, as shown in Figure 12.
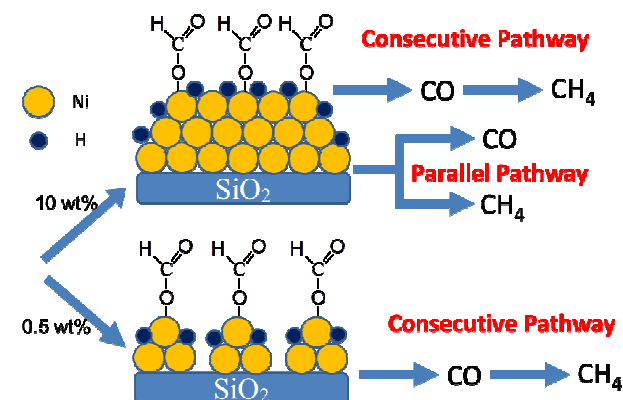
Figure 12 Propose mechanism for CO_2 hydrogenation on Ni/SiO_2.

The TPD profiles and IR spectra have unambiguously indicated that the m-HCOO intermediate is intricately involved in CO_2 hydrogenation over both the 0.5 wt% and 10 wt% Ni/SiO_2 catalysts, following the consecutive and parallel reaction pathways, respectively. On the 9-nm Ni particles (10 wt% Ni/SiO_2), in situ FT-IR studies revealed that the m-HCOO intermediate may form from co-adsorbed H_2 and CO_2 (Figure 8). The m-HCOO intermediate may directly convert to CO at increased temperatures. It was typically difficult to identify the formation of CH_4 by IR spectroscopy, but the TPD profiles of the 10 wt% Ni/SiO_2 catalysts post-reaction provided several clues regarding the particular formate intermediate associated

with CH_4 formation. The TPD results for the dissociation of residual species from the surfaces of large Ni particles detected simultaneous desorption of CH_4 and CO at 525 K (Figure 11), implying that CO and CH_4 are generated from the decomposition of residual species. The residual species on Ni surface was reasonably deduced to be the m-HCOO intermediate, based on assignment of the IR spectra. Thus, it is likely that CH_4 formation resulting from CO_2 hydrogenation is closely related to the m-HCOO intermediate. In fact, the TPD spectra of formic acid desorbed from the 10 wt% Ni/SiO$_2$ catalyst (Figure S4) also exhibited evidence for the direct conversion of adsorbed formic acid to CO and CH_4 at the same temperature. Thus, the parallel reactions at work in CO_2 hydrogenation on large Ni particles might involve the initial formation of the m-HCOO intermediate and subsequent competitively hydrogenation to CO or CH_4.

When the Ni loading was decreased to 0.5 wt%, CO_2 hydrogenation on the small Ni particles was attributed a consecutive reaction pathway where CO was the major intermediate in CH_4 formation. The IR spectra of H_2 and CO_2 co-adsorbed on the 0.5 wt% Ni/SiO$_2$ catalyst at different temperatures presented similar results to the those recorded in the experiments on the 10 wt% Ni/SiO$_2$ catalyst, indicating the formation of a m-HCOO species that was converted to CO. This result suggested that the m-HCOO species might be the key intermediate for CO_2 hydrogenation on small Ni particles. Interestingly, this consecutive pathway was closely related to the results of the TPD experiments on the post-hydrogenation materials, i.e., no CH_4 was observed from formate decomposition. A similar phenomenon, which was in agreement with the TPD spectra of formic acid on the 0.5 wt% Ni/SiO$_2$ catalyst, was the weak intensity of the CH_4 desorption peak. However, no obvious evidence for carbon deposition was observed on the 0.5 wt% and 10 wt% Ni/SiO$_2$ catalysts in our experiments. The carbon balance was higher than 95% of the carbon input. No Raman signals indicative of carbon deposition were found on the Ni/SiO$_2$ catalysts after undergoing long-term tests at 673 K for 48 h. This result suggested that the CH_4 formation did not follow a mechanism involving CO dissociation to a carbon species, followed by hydrogenation to CH_4.

The experimental results in this study indicate that the formation of a m-HCOO intermediate in an essential step in the co-adsorption of H_2 and CO_2 on both the 0.5 wt% or 10 wt% Ni/SiO$_2$ surfaces. The m-HCOO intermediate may be converted into CO via a dissociation process or be directly hydrogenated to CH_4 on the 10 wt% Ni/SiO$_2$ catalyst. Notably, the decomposition of the m-HCOO intermediate to CO might be the major reaction pathway on the 0.5 wt% Ni/SiO$_2$ catalyst. This would allow for only a small likelihood of direct hydrogenation of a m-HCOO intermediate to CH_4 on the small Ni particles. The difference between the reaction pathways on the two Ni/SiO$_2$ catalysts is likely dependent on the large difference between the Ni surface areas. Comparing the intrinsic reaction rate for CO_2 hydrogenation on the Ni/SiO$_2$ catalysts, the turnover rate of CO formation is always significantly higher for CH_4 formation. The TPD of formic acid

from the 0.5 wt% and 10 wt% Ni/SiO$_2$ surfaces indicated the possibility that the amount of CH_4 generated from the formate species was much lower than the CO formed. Therefore, the reaction of the m-HCOO intermediate on both Ni/SiO$_2$ catalysts prefers the formation of CO through a dissociation process rather than hydrogenation to CH_4.

The 10 wt% Ni/SiO$_2$ catalyst featured more active sites for CO_2 adsorption than the 0.5 wt% Ni/SiO$_2$ material, as confirmed by the CO_2-TPD profiles in Figure 9, where the ratio of the intensities of CO_2 desorption from 0.5 wt% to 10 wt% was ~0.37. It was noteworthy that the 0.5 wt% Ni/SiO$_2$ likely contained minimal H_2 adsorbed on the Ni surface, leading to the nearly unobservable desorption band in Figure 10. The reaction rate for the hydrogenation of the m-HCOO intermediate to CH_4 likely depends on the H_2 coverage of the Ni surface. The m-HCOO intermediate adsorbed on a small Ni particle may tend toward rapid formation of CO due to low H_2 surface coverage, showing a preference for the consecutive pathway and selectivity for CO formation. The 10 wt% Ni/SiO$_2$ material may provide stronger H_2 adsorption, leading to enhancements in H_2 coverage and in the likelihood of hydrogenation of the m-HCOO intermediate to CH_4. Such reasoning offers a justification for the possibility for the parallel pathway on large Ni particles.

We used CO as a probe molecule to identify the active phase on the reduced Ni/SiO$_2$ catalysts due to its characteristic vibrational signal, which can provide information related to the surface sites of an adsorbed species and the chemical environment of a Ni surface through vibrational spectroscopy. Figure S5 compares the IR spectra of CO adsorbed on the 0.5 wt% and 10 wt% Ni/SiO$_2$ catalysts at room temperature. The IR bands at frequencies greater than 2000 cm^{-1} were assigned to the adsorption of linear CO on the Ni surfaces. Monitoring the CO adsorbed on the 0.5 wt% or 10 wt% Ni/SiO$_2$ catalysts revealed broadened IR bands primarily centered at ~2060 cm^{-1}. The vibrational spectra of CO adsorbed on Ni(111) and Ni(100) surfaces have been reported in the literature, showing the occurrence of the stretching vibration of terminally bonded CO on low-index Ni surfaces in the range of 2017-2024 cm^{-1}.[59-63] The vibrational frequency might be expected at higher wavenumbers (~2057 cm^{-1}) on rough Ni-surfaces because of the numerous step-sites.[64] However, the observation of a vibrational frequency for linear CO adsorbed on Ni/SiO$_2$ is normally thought to fall in the range of 2040-2070 cm^{-1}.[65,66] In this study, the band at 2060 cm^{-1} was assigned to CO preferentially bound to low coordinate Ni atoms located at kink, corner or step positions.[66,67] The IR peaks of CO observed after H_2 and CO_2 co-adsorption on the 10 wt% and 0.5 wt% Ni/SiO$_2$ catalysts at 473 K were also observed at ~2060 cm^{-1} (Figures 8 and S1). Thus, it is reasonable that the adsorbed CO IR peak at 2060 cm^{-1} may directly result from the hydrogenation of CO_2 adsorbed on low coordinate Ni sites. These results implied that the metals situated at kink, corner or step positions were the primary active sites for CO_2 hydrogenation.

4. Experimental

4.1 Catalyst preparation

The Ni/SiO_2 catalysts were prepared by impregnating 1 g samples of SiO_2 (Sigma-Aldrich, 300 m^2/g) with 20 mL of 8.5×10^{-2} M and 4.3×10^{-3} M aqueous $Ni(NO_3)_2$ to prepare 10 wt% and 0.5 wt% Ni catalysts, respectively. All of the Ni catalysts were calcined in air and reduced under H_2 at 773 K for 5 h before use.

4.2 Measurement of the FT-IR spectra

The in situ DRIFT analyses of materials after H_2 and CO_2 co-adsorption were performed using a Nicolet 5700 FTIR spectrometer equipped with a mercury cadmium telluride (MCT) detector with a $1\,cm^{-1}$ resolution for 256 scans. The DRIFT cell (Harrick) was equipped with ZnSe windows and a heating cartridge that allowed for heating of the sample to 773 K. The IR spectra of the Ni/SiO_2 catalysts after H_2 and CO_2 adsorption were obtained after passing CO_2 through the Ni/SiO_2 samples for 30 min at room temperature. Residual gaseous CO_2 was purged for 60 min using a He stream, followed by a H_2 stream for reaction with the Ni/SiO_2 samples containing adsorbed CO_2. The IR spectra were recorded in a H_2 stream at elevated temperature. The IR spectra of the Ni/SiO_2 catalysts with adsorbed CO were obtained by passing a stream of CO through the Ni/SiO_2 samples for 30 min at room temperature. The residual gaseous CO was purged for 60 min using a He stream.

4.3 Measurement of the nickel surface area

The Ni surface areas of the Ni/SiO_2 catalysts were measured via saturated CO chemisorption at room temperature in a glass vacuum system. The gas pressure is measured by a Granville Phillips 375 Convectron Vacuum Gauge. All Ni catalysts were calcined in air and reduced under H_2 at 773 K for 5 h prior to CO chemisorption. The Ni sample disk was composed of 0.2 g of catalyst pressed at 260 atm, which was repeatedly reduced in 760 Torr of H_2 at 773 K for 2 h and evacuated at 773 K and 4×10^{-5} Torr in the glass vacuum system for 30 min. The catalyst was treated with 20 Torr of CO at room temperature for 10 min to ensure uptake saturation. The surface area of the Ni catalyst was calculated assuming a CO/Ni stoichiometric ratio of 1. The average surface density of the Ni metal was 1.54×10^{19} Ni $atoms/m^2$.

4.4 X-Ray diffraction (XRD) measurements

The XRD measurements for all of the Ni/SiO_2 samples were performed at the high-energy beamline 01C2 at the National Synchrotron Radiation Research Center (NSRRC), Hsinchu. The beamline was operated at 25 keV, and the XRD spectra were recorded at a wavelength of λ = 0.1549 nm. The samples were loaded into a capillary cell that could be heated to 773 K under a flow of H_2 gas while the XRD patterns were recorded.

4.5 Catalytic CO_2 hydrogenation tests

All CO_2 hydrogenation reactions were performed in a fixed-bed reactor (0.95 cm inner diameter) at atmospheric pressure. A thermocouple connected to a PID temperature controller was placed on top of the catalyst bed. Catalyst samples (50 mg) were used in all of the CO_2 hydrogenation reactions, which were conducted by treating the catalyst with a stream of H_2/CO_2. The conversion rate of the reaction was maintained at less than 10% to ensure that the conditions were similar to differential conditions. All products were analyzed via gas chromatography (GC) through a 12-ft Porapak-Q column. The gas chromatograph was equipped with a thermal conductivity detector (TCD). The turnover frequency (TOF) was calculated using the following formula: TOF=[conversion×CO_2 flow rate (mL/s)×6.02 ×10^{23} (molecules/mol)]/[24400 (mL/mol)×Ni sites]. Carbon balance data were measured from the peak areas corresponding to CH_4 and CO in the chromatograms throughout the experiment over the temperature range, which were good at approximately 95-100%.

4.6 Temperature-programmed desorption (TPD)

The H_2- and CO_2-TPD experiments were performed using a 100 mL/min stream of He at atmospheric pressure in a fixed-bed flow system. The H_2 and CO_2 streams (100 mL/min) were fed over the catalysts for 1 h at room temperature to achieve saturation. The temperature was increased from 300 to 800 K at a rate of 10 K/min over the course of the TPD process. The signals corresponding to H_2 (m/z 2 amu) and CO_2 (m/z 44 amu) were measured with a VG Smart IQ+ 200D mass spectrometer. The temperature was measured with a K-type thermocouple inserted into the catalyst bed, and the desorbed products were carried to the vacuum chamber through a leak valve using He as the carrier gas. The operating pressure in the chamber was approximately 3×10^{-7} mbar, and the base pressure in the chamber was approximately 5×10^{-10} mbar. Formic acid was added to all of the catalysts by injection with a 10-μL Hamilton 7001 syringe through a port located upstream of the quartz reactor. The injection port, similar to that used in gas chromatography, was heated to 373 K to prevent the condensation of liquid.

4.7 Transmission electron microscopy (TEM)

High-resolution TEM analyses were performed on a JeJEOL-JEM3000F instrument located at the High Valued Instrument Center of the National Tsing Hua University, Taiwan. The instrument was operated at 300 keV. After the pre-treatment of the catalyst samples, they were dispersed in methanol and ultrasonically mixed at room temperature. A portion of this solution was dropped onto a Cu grid for TEM imaging.

4.8 H_2 temperature-programmed reduction (H$_2$-TPR)

H_2-TPR of the catalysts was performed at atmospheric pressure in a conventional flow system. The Ni/SiO_2 catalyst was placed in a tube reactor and heated at a rate of 10 K/min in a 10% H_2/N_2 mixed gas stream flowing at 30 mL/min. The TCD current was 80 mA and the detector temperature was 373 K. A cold trap containing a gel formed by the addition of liquid nitrogen to isopropanol in a thermos flask was used to prevent water from entering the TCD.

5. Conclusion

In this paper, the kinetic parameters, reaction pathways, reaction intermediates and selectivity for catalytic CO_2

hydrogenation were investigated on Ni/SiO_2 catalysts with dramatically different Ni loadings. We have clearly shown that CO_2 hydrogenation proceeds via different reaction pathways depending on the Ni particle size. The m-HCOO intermediate is intricately involved in CO_2 hydrogenation with both Ni/SiO_2 catalysts, regardless of the Ni loading and particle size. At low Ni loading (0.5 wt%), the catalyst provided higher catalytic activity for CO_2 hydrogenation than the 10 wt% Ni/SiO_2 catalyst. CO_2 hydrogenation likely follows a consecutive pathway on the 0.5 wt% Ni/SiO_2 catalyst, forming CO and CH_4. However, the low H_2 coverage on small Ni particles leads to the quick formation of CO from the m-HCOO intermediate. This process led to high selectivity for CO formation on the 0.5 wt% Ni/SiO_2 catalyst. When the Ni loading was increased to 10 wt% (ca. 9-nm particles), the selectivity switched to favor CH_4 formation, and the reaction proceeds through the mixed consecutive and parallel pathways. The parallel reaction pathway may involve competitive dissociation to CO or hydrogenation to CH_4 of the m-HCOO intermediate. The 10 wt% Ni/SiO_2 material has more active sites for H_2 adsorption than the 0.5 wt% Ni/SiO_2 catalyst, resulting in higher H_2 coverage on the Ni surface, further enabling the parallel pathway. The sites corresponding to kink, corner or step positions are proposed as the primary active sites for CO_2 hydrogenation on both Ni/SiO_2 catalysts.

Acknowledgements

Notes and references

[a]Center for General Education, Chang Gung University, 259, Wen-Hua 1st Rd., Guishan Dist., Taoyuan City 33302, Taiwan, Republic of China
*Corresponding author
E-mail: cschen@mail.cgu.edu.tw
Tel.: +886-32118800x5685
Fax: +886-32118700
[b]Taiwan Power Research Institute, 84, Ta-An Road, Shu-LinTaipei New City 23847 Taiwan, Republic of China
[c]Department of Materials Science, National University of Tainan, 33, Sec. 2, Shu-Lin St., Tainan 700, Taiwan, Republic of China

1   X. Xiaoding and J.A. Moulijn, *Energy Fuels* 1996, **10**, 305-325.
2   P.G. Jessop, T. Ikariya and R. Noyori, *Chem. Rev.* 1995, **95**, 259-270.
3   C.C. Tai, J. Pitts, J.C. Linehan, A.D. Main, P. Munshi and P.G. Jessop, *Inorg. Chem.* 2002, **41**, 1606-1614.
4   Y. Ohnishi, T. Matsunaga, Y. Nakao, H. Sato and S. Sakaki, *J. Am. Chem. Soc.* 2005, **127**, 4021-4032.
5   P. Munshi, A.D. Main, J.C. Linehan, C.C. Tai and P.G. Jessop, *J. Am. Chem. Soc.* 2002, **124**, 7963-7971.
6   B. Chan and L. Radom, *J. Am. Chem. Soc.* 2008, **130**, 9790-9799.
7   D.Y. Hwang and A.M. Mebel, *J. Phys. Chem. A* 2004, **108**, 10245-10251.
8   J. Yoshihara, S.C. Parker, A. Schafer and C.T. Campbell, *Catal. Lett.* 1995, **31**, 313-324.
9   I. Nakamura, T. Fujitani, T. Uchijima and J. Nakamura, *Surf. Sci.* 1998, **400**, 387-400.
10   C.S. Chen, J.H. Lin, J. H. You and C.R. Chen, *Am. Chem. Soc.* 2006, **128**, 15950-15951.
11   C.S. Chen, W.H. Cheng and S.S. Lin, *Appl. Catal. A* 2004, **257**, 97-106.
12   C.S. Chen, W.H. Cheng and S.S. Lin, S.S. *Appl. Catal. A* 2003, **238**, 55-67.
13   C.S. Chen and W.H. Cheng, *Catal. Lett.* 2002, **83**, 121-126.
14   C.S. Chen, W.H. Cheng and S.S. Lin, *Catal. Lett.* 2000, **68**, 45-48.
15   C.S. Chen, W.H. Cheng and S.S. Lin, *Chem. Commun.* 2001, 1770-1771.
16   E. Vesselli, L.D. Rogatis, X. Ding,; A. Baraldi, L. Savio, L. Vattuone,; M. Rocca, P. Fornasiero, M. Peressi, A. Baldereschi, R. Rosei and G. Comelli, *J. Am. Chem. Soc.* 2008, **130**, 11417-11422.
17   T. Fujitani, I. Nakamura, T. Uchijima and J. Nakamura, *Surf. Sci.* 1997, **383**, 285-298.
18   Z. Zhang, A. Kladi and X.E. Verykios, *J. Catal.* 1994, **148**, 737-747.
19   M.A. Henderson and S.D. Worley, *J. Phys. Chem.* 1985, **89**, 1417-1423.
20   C. Schild, A. Wokaun, R.A. Koeppel and A. Baiker, *J. Phys. Chem.* 1991, **95**, 6341-6346.
21   M.J.L. Ginés, A.J. Marchi and C.R. Apesteguía, *Appl. Catal. A* 1997, **154**, 155-171.
22   W. Wang, S. Wang, X. Ma and J. Gong, *Chem. Soc. Rev.* 2011, **40**, 3703-3727.
23   J.R. Khusnutdinova, J.A. Garg and D. Milstein, *ACS Catal.* 2015, **5**, 2416–2422.
24   K. Tsuchiya, J.D. Huang and K.I. Tominaga, *ACS Catal.* 2013, **3**, 2865–2868.
25   O.A. Baturina, Q. Lu, M.A. Padilla, L. Xin, W. Li, A. Serov, K. Artyushkova, P. Atanassov, F. Xu, A. Epshteyn, T. Brintlinger, M. Schuette and G.E. Collins, *ACS Catal.* 2014, **4**, 3682–3695.
26   G.A. Filonenko, D. Smykowski, B.M. Szyja, G. Li, J. Szczygieł, E.J.M. Hensen and E.A. Pidko, *ACS Catal.* 2015, **5**, 1145–1154.
27   R. Grabowski, J. Słoczyński, M. Śliwa, D. Mucha, R.P. Socha, M. Lachowska and J. Skrzypek, *ACS Catal.* 2011, **1**, 266–278.
28   G.A. Filonenko, M.P. Conley, C. Copéret, M. Lutz, E.J.M. Hensen and E.A. Pidko, *ACS Catal.* 2013, **3**, 2522–2526.
29   S. Natesakhawat, J.W. Lekse, J.P. Baltrus, P.R. Ohodnicki, Jr., B.H. Howard, X. Deng and C. Matranga, *ACS Catal.* 2012, **2**, 1667–1676.
30   K. Samson, M. Śliwa, R.P. Socha, K. Góra-Marek, D. Mucha, D. Rutkowska-Zbik, J-F. Paul, M. Ruggiero-Mikołajczyk, R. Grabowski and J. Słoczyński, *ACS Catal.* 2014, **4**, 3730–3741.
31   J.H. Kwak,; L. Kovarik and J. Szanyi, J. *ACS Catal.* 2013, **3**, 2449–2455.
32   J.H. Kwak,; L. Kovarik and J. Szanyi, *ACS Catal.* 2013, **3**, 2094–2100.
33   M.A.A. Aziz, A.A. Jalil, S. Triwahyono, R.R. Mukti, Y.H. Taufiq-Yap and M.R. Sazegar, *Appl. Catal. B* 2014, **147**, 359-368.
34   A. Karelovic and P. Ruiz, *ACS Catal.* 2013, **3**, 2799–2812.
35   E. Vesselli, J. Schweicher, A. Bundhoo, A. Frennet and N. Kruse, *J. Phys. Chem. C* 2011, **115**, 1255–1260.
36   G. Du, S. Lim, Y. Yang, C. Wang, L. Pfefferle and G.L. Haller, *J. Catal.* 2007, **249**, 370-379.
37   D. Theleritis, S. Souentie, A. Siokou, A. Katsaounis and C.G. Vayenas, *ACS Catal.* 2012, **2**, 770–780.

38 T.C. Schilke, I.A. Fisher and A.T. Bell, *J. Catal.* 1999, **184**, 144-156.
39 N. Nomura, T. Tagawa and S. Goto, *Appl. Catal. A* 1998, **166**, 321-326.
40 M. Wisniewski, A. Boréave and P. Gélin, *Catal. Commun.* 2005, **6**, 596-600.
41 E. Ruckenstein and Y.H. Hu, *J. Catal.* 1996, **162**, 230-238.
42 Y.G. Chen, K. Tomishige, K. Yokoyama and K. Fujimoto, *J. Catal.* 1999, **184**, 479-490.
43 S. Zhang, J. Wang, H. Liu and X. Wang, *Catal. Commun.* 2008, **9**, 995-1000.
44 N. İnoğlu and J. R. Kitchin, *J. Catal.* 2009, **261**, 188-194.
45 S.I. Fujita, M. Usui and N. Takezawa, *J.Catal.* 1992, **134**, 220-225.
46 I. Rossetti, C. Biffi, C.L. Bianchi, V. Nichele, M. Signoretto, F. Menegazzo, E. Finocchio, G. Ramis and A.D. Michele, *Appl. Catal. B* 2012, **117-118**, 384–396.
47 F. Arena, G. Mezzatesta, G. Zafarana, G. Trunfio, F. Frusteri and L. Spadaro, *J. Catal.* 2013, **300**, 141–151.
48 E. Vesselli, M. Rizzi, L.D. Rogatis, X. Ding, A. Baraldi, G. Comelli, L. Savio, L. Vattuone, M. Rocca, P. Fornasiero, A. Baldereschi and M. Peressi, *J. Phys. Chem. Lett.* 2010, **1**, 402–406.
49 E. Vesselli, L.D. Rogatis, X. Ding, A. Baraldi, L. Savio, L. Vattuone, M. Rocca, P. Fornasiero, M. Peressi, A. Baldereschi, R. Rosei and G. Comelli, *J. Am. Chem. Soc.* 2008, **130**, 11417–11422.
50 A. Bandara, J. Kubota, A. Wada, K. Domen and C. Hirose, *J. Phys. Chem. B* 1997, **101**, 361–368.
51 A. Bandara, J. Kubota, A. Wada, K. Domen and C. Hirose, *J. Phys. Chem.* 1996, **100**, 14962–14968.
52 A. Yamakata, J. Kubota, J.N. Kondo, K. Domen and C. Hirose, *J. Phys. Chem.* 1996, **100**, 18177–18182.
53 B. Qiao, A. Wang, X. Yang, L.F. Allard, Z. Jiang, Y.Cui, J. Liu, J. Li and T. Zhang, *Nature Chem.* 2011, **3**, 634.
54   M. Moses-DeBusk, M. Yoon, L.F. Allard, D.R. Mullins, Z. Wu, X. Yang, G. Veith, G.M. Stocks and C.K. Narula, *J. Am. Chem. Soc.* 2013, **135**, 12634.
55 D. Mei, V.M. Lebarbier, R. Rousseau, V.A. Glezakou, K.O. Albrecht, L. Kovarik, M. Flake and R.A. Dagle, *ACS Catal.* **2013**, **3**, 1133.
56 Y.T. Lai, T.C. Chen, Y.K. Lan, B.S. Chen, J.H. You, C.M. Yang, N.C. Lai, J.H. Wu and C.S. Chen, *ACS Catal.* 2014, **4**, 3824-3836.
57 C. Schild, A. Wokaun, R.A. Koeppel and A. Baiker, *J. Phys. Chem.* 1991, **95**, 6341–6346.
58 O. Levenspiel, *Chemical Reaction Engineering*, Wiely, New York, 2nd edn., 1972, ch8, p238.
59 K. Sinniah, H. E. Dorsett and J.E. Reutt-Robey, *J. Chem. Phy.* 1993, 98, 9018-9029.
60 A. Grossmann, W. Erley and H. Ibach, *Surf. Sci.* 1996, **355**, L331–L334.
61 G. Chiarello, A. Cupolillo, C. Giallombardo, R.G. Agostino, V. Formoso, D. Pacilè, L. Papagno and E. Colavita, *Surf. Sci.* 2003, **536**, 33–44.
62 D. Pacilè, M. Papagno, G. Chiarello, L. Papagno and E. Colavita, *Surf. Sci.* 2004, **558**, 89–98.
63 A. Politano and G. Chiarello, *J. Phys. Chem. C* 2011, **115**, 13541–13553
64 K. Svensson, I. Rickardsson, C. Nyberg and S. Andersson, *Surf. Sci.* 1996, **366**, 140–148.
65 K.A. Layman and M.E. Bussell, *J. Phys. Chem. B* 2004, **108**, 10930–10941.
66 M.L. Ang, U. Oemar, E.T. Saw, L. Mo, Y. Kathiraser, B.H. Chia and S. Kawi, *ACS Catal.* 2014, **4**, 3237–3248.
67 M. Agnelli, H.M. Swaan, C. Marquez-Alvarez, G.A. Martin and C. Mirodatos, *J. Catal.* 1998, **175**, 117-128.